Wei et al. Advances in Aerodynamics (2023) 5:16
https://doi.org/10.1186/s42774-023-00146-0

Advances in Aerodynamics

RESEARCH

Open Access

Experimental and numerical study on dynamic stall under a large Reynolds number

Binbin Wei[1*], Yongwei Gao[2] and Shuling Hu[1]

*Correspondence:
weibinbin@xjtu.edu.cn

[1] School of Aerospace Engineering, Xi'an Jiaotong University, Xi'an 710049, China
[2] School of Aeronautics, Northwestern Polytechnical University, Xi'an 710072, China

Abstract

Dynamic stall under large Reynolds numbers and large reduced frequencies has a significant effect on the performance of the wind turbine blades, helicopter rotors, etc. So the dynamic stall physics of the NACA0012 airfoil under a large Reynolds number of $Re = 1.5 \times 10^6$ was studied using experimental and numerical methods. The reduced frequency range was $k = 0.035 - 0.1$. The unsteady flow field in dynamic stall was studied in detail by using the transient pressure measurement and the numerical simulation based on the unsteady Reynolds-averaged Navier-Stokes (URANS) equation. And the time-frequency characteristics of the dynamic stall were studied using the wavelet analysis. The study showed that the aerodynamic performance during the dynamic stall was dominated by the shear layer vortex (SLV) and the leading edge vortex (LEV), and the phase difference between the SLV and the LEV was the key factor in the existence of the bimodal characteristics of the aerodynamic force/moment. There was a significant linear correlation between the negative peak of the vortex-induced C_p and the C_n in the reduced frequency range studied in this paper. During the convection of the near-wall LEV to the trailing edge, the high-frequency features firstly decay, and the multi-scale structures of the LEV become more significant as the reduced frequency gradually increases.

Keywords: Dynamic stall, Dynamic stall vortex (DSV), Leading edge vortex (LEV), Time-frequency analysis, Wavelet analysis

1 Introduction

Dynamic stall phenomena are widely present in nature and engineering. In nature, the flight of insects and birds is directly related to the dynamic stall phenomenon of wings, and the swimming of fish in water is also related to the dynamic stall phenomenon of fish tails and fin surfaces. In engineering, the dynamic stall occurs in small/medium/large wind turbine blades, helicopter rotors, etc. Whether from purely academic research or from practical engineering applications, there is a need to conduct in-depth research on dynamic stall phenomena.

It is generally believed that the formation and development of the strong coherent structure called dynamic stall vortex (DSV) directly affects the dynamic stall. Before the start of dynamic stall, a very thin reversed-flow area is formed at the trailing edge. Owing to the reverse pressure gradient, the reversed-flow area gradually moves to the leading edge. During this process, the flow remains attached. As the vorticity accumulates at the leading edge, a leading-edge vortex (LEV) that creates strong suction at the leading edge is formed. When the LEV cannot maintain the existing scale, it will detach from the leading edge of the airfoil and convect downstream, forming the DSV. So the LEV can be considered as the initial stage of DSV [1], and it is thought to be the key flow structure in dynamic stall [2].

Depending on the actual situation, the Reynolds number and reduced frequency of dynamic stall generally vary greatly. The Reynolds number and the reduced frequency are two important non-dimensional parameters to describe the pitching oscillation motion, and they are two very important similarity criteria that affect the dynamic stall characteristics. The Reynolds number is defined as $Re = \rho Uc/\mu$, where ρ is the fluid density, U is the free-stream velocity, c is the characteristic scale, and μ is the free-stream viscosity. The reduced frequency is defined as $k = \pi fc/U$ and indicates the ratio of the convective time scale to the forced oscillation time scale. Here f is the motion frequency. The Reynolds number on the flying insect wings is generally in the order of 10^3, and the laminar separation occurs at this Reynolds number. The dynamic stall of large flying birds and micro air vehicles (MAV) generally occurs in the Reynolds number of the order of 10^4. Small to medium wind turbine blades often work in the Reynolds number of the order of 10^5. And the dynamic stall of large wind turbine blades and helicopter rotors is generally in the Reynolds number beyond the order of 10^6, which is dominated by the turbulent separation.

When the dynamic stall occurs, the unsteady characteristics of the flow field increase significantly, resulting in nonlinear changes in the aerodynamic forces and moments. The strongly unsteady nature of the dynamic stall makes it difficult to predict or simulate accurately, so the wind tunnel experiments are often conducted. For large wind turbine blades and helicopter blades, the operating environment is generally a situation of large Reynolds number and large reduced frequency. However, it is not easy to simulate the Reynolds number and reduced frequency simultaneously in the wind tunnel experiment. A high Reynolds number requires a large Uc, while a high reduced frequency requires a large fc/U. Therefore, in order to simulate the large Reynolds number and large reduced frequency simultaneously, both f, c and U need to be set to large values, which requires a large wind tunnel scale and strong dynamic mechanism capability. This puts forward high requirements for the wind tunnel experiment capability.

We have summarized several studies on dynamic stall [3–38] as shown in Fig. 1. It can be seen that the Reynolds number and the reduced frequency roughly show a negative correlation, which is related to the actual working environment of the research subject, and also limited by the actual simulation capability of the computational fluid dynamics (CFD) and wind tunnel experiment. As can be seen from the figure, few experimental studies can satisfy both the experimental conditions of Reynolds number of the order of 10^6 and reduced frequency of the order of 10^{-1}. This cannot meet the working conditions of large Reynolds number and large reduced frequency for the large wind turbine blades and the helicopter blades.

To this end, we conducted a study on the dynamic stall of the NACA0012 airfoil under a large Reynolds number ($Re \sim O(10^6)$) and a large reduced frequency ($k \sim O(10^{-1})$). The experimental Reynolds number was $Re = 1.5 \times 10^6$, and the reduced frequencies were

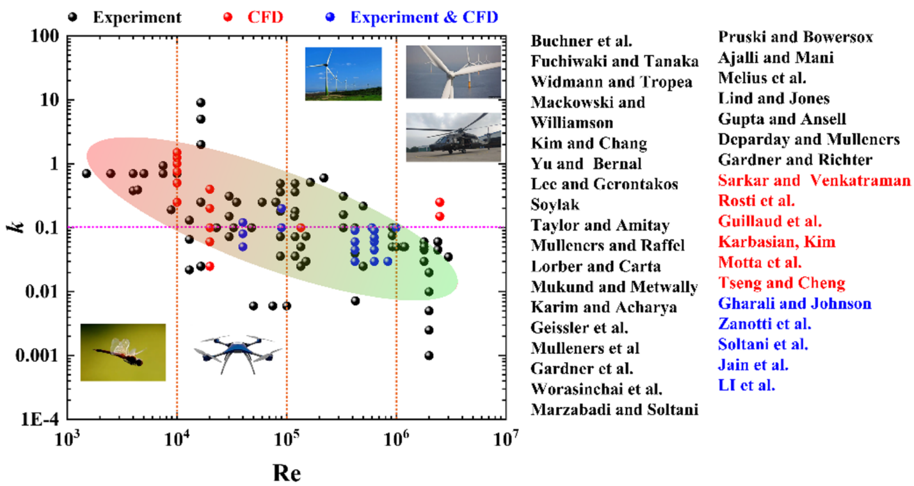

Fig. 1 Distribution of the Reynolds number and reduced frequency for dynamic stall studies [3–38]

$k = 0.035$, 0.05 and 0.1. The evolutions of the unsteady flow field at different reduced frequencies were studied in detail. The vortex characteristics of the dynamic stall were studied in depth. And a time-frequency analysis on the dynamic stall was conducted at the end of the article.

2 Experimental and numerical setup

2.1 Experimental setup and procedures

The experiment was conducted in the NF-3 wind tunnel at Northwestern Polytechnical University, China. The size of the airfoil test section is $8.0\,\text{m} \times 1.6\,\text{m} \times 3.0\,\text{m}$ (length $\times$ height $\times$ width). The maximum wind speed is $U = 130\,\text{m/s}$ and the turbulence intensity is less than 0.05%.

In order to meet the demand of high Reynolds number and high reduced frequency during the service of large wind turbine blades and helicopter rotors, the airfoil oscillation drive mechanism of the NF-3 wind tunnel has been modified in recent years. At present, the drive mechanism can realize three types of motion, including the pitching oscillation, plunging oscillation and pitching-plunging coupled oscillation. The pitching oscillation frequency could be controlled in the range of $f = 0 - 5\,\text{Hz}$. The maximum angular amplitude was $A_{max} = 15°$ and the average angle of attack (AoA) was $\alpha = 0° - 360°$ with an accuracy of $\varepsilon \leq 6'$.

The unsteady pressure on the airfoil surface was measured using the Kulite XCQ-093 dynamic pressure sensor, and the signals of the sensors were collected by the VXI data acquisition system. The system possesses 48 acquisition channels with acquisition accuracy of 16 bit analog-to-digital (A/D) and a sampling frequency of not less than 100 kHz/channel.

The chord length and span length of the NACA0012 airfoil model were $c = 700\,\text{mm}$ and $l = 1600\,\text{m}$, respectively. The rotation axis was located at the position of $x/c = 0.25$. Thirty-two Kulite XCQ-093 dynamic pressure sensors were arranged clockwise along the middle of the model ($z/l = 0.50$), including 16 on the upper surface, 14 on the lower surface, and one on each of the leading and trailing edges, as shown in Fig. 2.

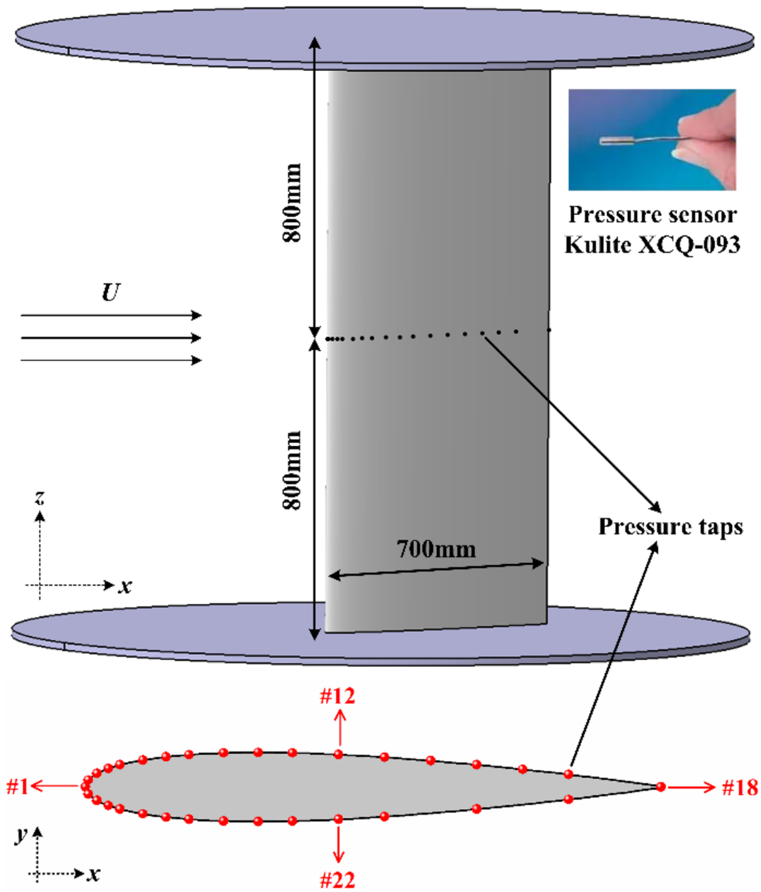

Fig. 2 Schematic diagram of the airfoil dynamic drive mechanism

Dynamic stall generally starts from the occurrence of the LEV, and ten pressure taps were arranged at the leading edge of $x/c \leq 0.30$ on the suction surface to ensure sufficient spatial resolutions around the leading edge. The sampling rate of the experiment was set to $f_s = 20\,\text{kHz}$ to ensure a sufficiently high time accuracy.

In this experiment, the free flow velocity was $U = 31.7\,\text{m/s}$, and the chord length based Reynolds number was $Re = 1.5 \times 10^6$. To study the effects of the reduced frequency on the dynamic stall, the pitching oscillation frequencies were controlled to $f = 0.5$, 0.721 and 1.442, and the corresponding reduced frequencies were $k = \pi fc/U = 0.035$, 0.05 and 0.1 respectively. The motion of the model was set to a sinusoidal motion with an average AoA of $\alpha = 15°$and an amplitude of $A = 10°$.

The experimental data were processed using the period averaging or phase averaging method (PA) [2, 26, 39] and the slip window technique (SWT) [40]. The experimental data were guaranteed to be collected for at least 10 cycles for each reduced frequency. The pressure at the measurement points in each cycle was first calculated using the SWT, and then the aerodynamic force/moment of each cycle was calculated by the pressure integration. Then the averaged aerodynamic force/moment was calculated using the PA method.

In order to obtain the time-frequency characteristics of the near-wall DSV, the continuous wavelet transform (CWT) was used to analyze the experimental pressure [26, 41]. A wavelet basis function is a set of orthogonal bases in which frequency components of a certain bandwidth are distributed near the center frequency. The complex Morlet wavelets were used as the wavelet basis functions for CWT in this paper. The expression of the complex Morlet wavelets is as follows:

$$\psi(t) = \frac{1}{\sqrt{\pi f_b}} e^{i2\pi f_c t} e^{-t^2/f_b}, \tag{1}$$

where f_b is a bandwidth parameter and f_c is a wavelet center frequency.

2.2 Numerical setup and procedures

In this paper, the transient pressure field on the model surface was measured, while the velocity field around the dynamic airfoil was not measured using techniques such as the particle image velocimetry (PIV). Therefore, in order to better analyze the dynamic stall, a numerical simulation study on the two-dimensional NACA0012 airfoil was carried out in this paper. The chord length of the computational model was the same as the experimental model, which was $c = 700$ mm. The computational domain was square, and the side length of the computational domain was $80c$. In order to simulate the pitching oscillation motion of the airfoil, a circular domain was divided around the center of rotation of the airfoil. The center of this rotation domain is located at $x/c = 0.25$, and the diameter was 1800 mm, as shown in Fig. 3(a).

The structured mesh of the computational domain was calculated, and the height of the first grid was set to $10^{-5}c$ to ensure $y^+ \approx 1.0$. The global mesh of the computational

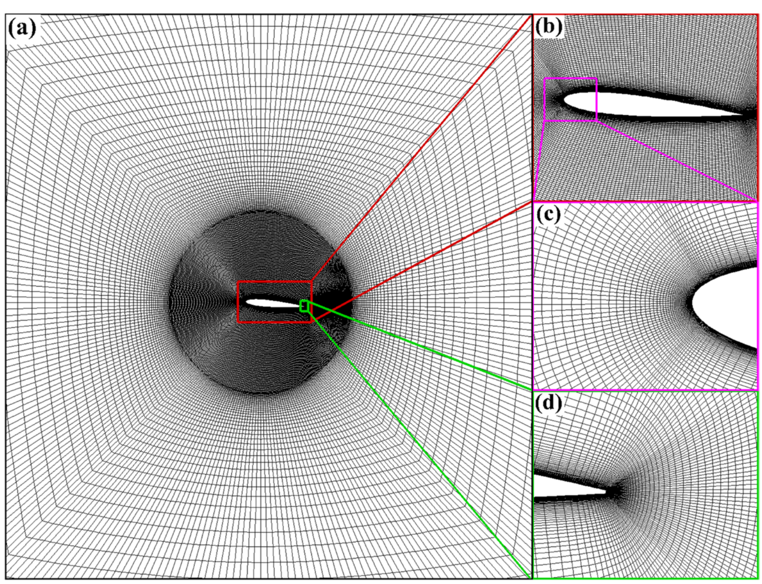

Fig. 3 Calculated mesh. **a** Global mesh, **b** mesh around the airfoil, **c** mesh at the leading edge, and **d** mesh at the trailing edge

domain, the mesh near the airfoil, and the mesh at the leading and trailing edge of the airfoil are shown in Fig. 3. The total number of nodes in this paper was 88,000 [33].

The unsteady Reynolds-averaged Navier-Stokes (URANS) equation was solved using the finite volume method (FVM), and the shear stress transport (SST) k-ω turbulence model was introduced to close the control equations. In the unsteady solution process, the control equation was solved by using the double time progression, and the pseudo time iteration adopted the multi-step Runge-Kutta scheme. The time step was set to $\Delta t = 1.5\times 10^{-4}T$ [2]. In this paper, the unsteady flow field was calculated for two reduced frequencies of $k = 0.035$ and 0.1, and the corresponding time steps were $dt = 3\times 10^{-4}$ s and 1×10^{-4} s, respectively. The calculated incoming velocity was $U = 31.7$ m/s, which was the same as the experimental conditions.

3 Results and analysis

3.1 Aerodynamic performance

The reliability of the experimental results and numerical calculations in this paper was firstly verified.

A comparison of the experimental results, the calculated results, and the experimental results of McAlister et al. [42] is shown in Fig. 4. The experimental data in Fig. 4(a) are calculated by the SWT method. And the experimental data of this paper in Fig. 4(b) are averaged during the last 15 cycles by the PA method, which can be used to evaluate the repeatability of the experiment. The black scatter points are the experimental results of McAlister et al. [42], and the red and blue solid lines are the experimental and calculated results in this paper, respectively. It can be seen from Fig. 4(b) that the errors of the normal force coefficient C_n between each cycle were small in the attached flow during the upstroke and downstroke, which indicated that the aerodynamic performance showed good periodicity. In the separated flow, the periodicity was not as good as that in the attached flow due to the strong unsteady properties, which was consistent with the physics of unsteady flow. The computational and experimental results are in overall agreement. There are differences between the two in the dynamic stall. And these differences can be attributed to the flow separation and the development of vortices. Specifically, the maximum of C_n of our computational results for $k = 0.035$ is larger than that of our experimental data. And our computational results for $k = 0.1$ show a bimodal feature, while the experimental results do not. And this part is analyzed in detail in

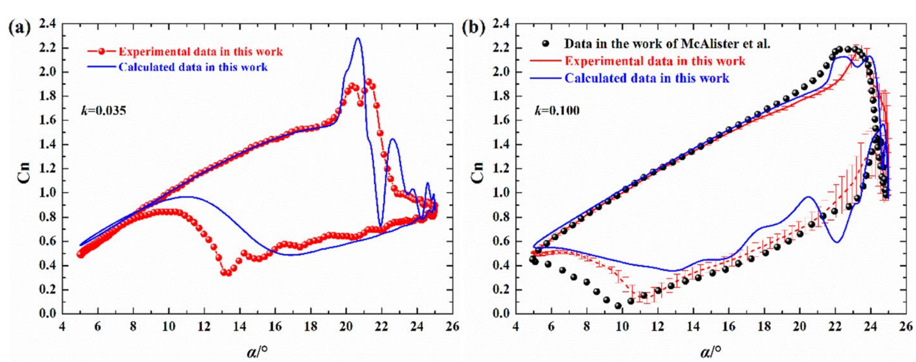

Fig. 4 Comparison of the experimental and computational C_n. **a** $k = 0.035$, **b** $k = 0.1$

Section 3.2. Comparing the experimental and calculated results in this paper with those of McAlister et al. [42], the experimental and calculated data in this paper are reliable.

The experimental normal force and moment coefficients under different reduced frequencies are shown in Fig. 5. The colors black, red and blue represent the reduced frequency of $k=0.035$, 0.05 and 0.1 respectively. The results in Fig. 5 are the results calculated by the SWT method within one cycle; therefore, there is a slight difference between the results in Fig. 4 and Fig. 5 for that the experimental results of $k=0.1$ in Fig. 4 are averaged by multiple cycles using the PA method. At large AoAs in the upstroke, the slope of the normal force line increased significantly compared with that at small AoAs, which was attributed to the occurrence of dynamic stall. As the reduced frequency gradually increased, the AoA at which the slope of the normal force line began to improve increased, the maximum C_n gradually increased, and the AoA corresponding to the maximum C_n gradually increased. The peak negative moment coefficient C_m also decreased with the gradual increase of the reduced frequency and exhibited a significant hysteresis characteristic. At AoAs in the downstroke, the flow reattachment occurred, characterized by a wide range of lift increase. As the reduced frequency increased, the AoA corresponding to the flow reattachment gradually decreased. The minimum C_n gradually reduced during the flow reattachment, reflecting the gradual weakening of the reattachment ability. This property was also reflected by the variation pattern of C_m. It can be seen that the reduced frequency has a significant effect on the dynamic stall and flow reattachment.

3.2 Unsteady pressure field evolution during dynamic stall

In this section, the evolution of the unsteady pressure field on the wall during dynamic stall for $k=0.035$ and 0.1 is studied. The experimental results in this section are the calculated results of the SWT method within one cycle.

3.2.1 Case of k = 0.035

The spatial-temporal evolution of the pressure coefficient C_p is an effective means to study the dynamic stall. The shear layer vortex (SLV) or turbulent separation vortex (TSV) [43], LEV [1], and DSV [26] can be identified by the spatial-temporal evolution of C_p. In the dynamic stall, the vortex-induced suction changes in position along with the

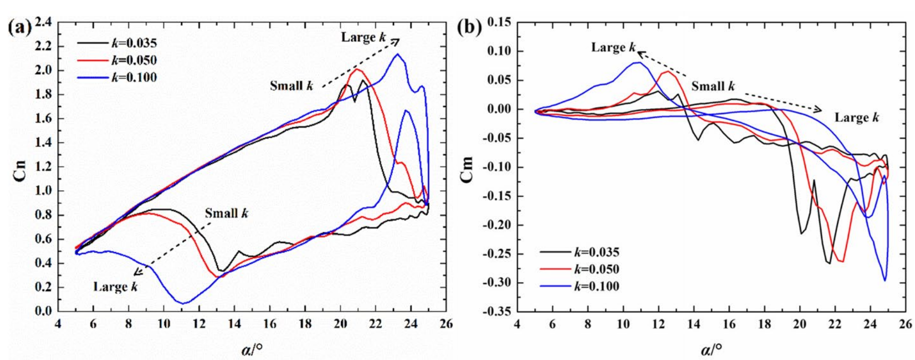

Fig. 5 Experimental aerodynamic performance at different reduced frequencies. **a** C_n, **b** C_m

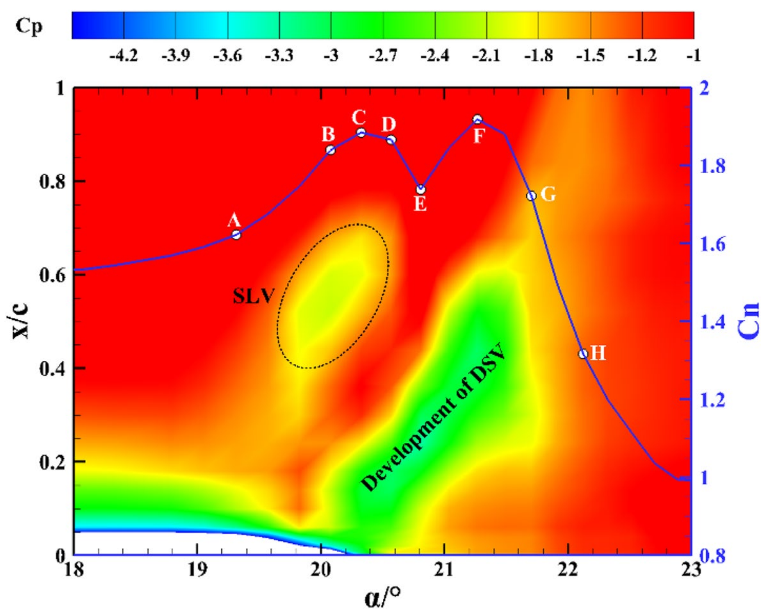

Fig. 6 Spatial-temporal evolution contours of C_p for $k=0.035$

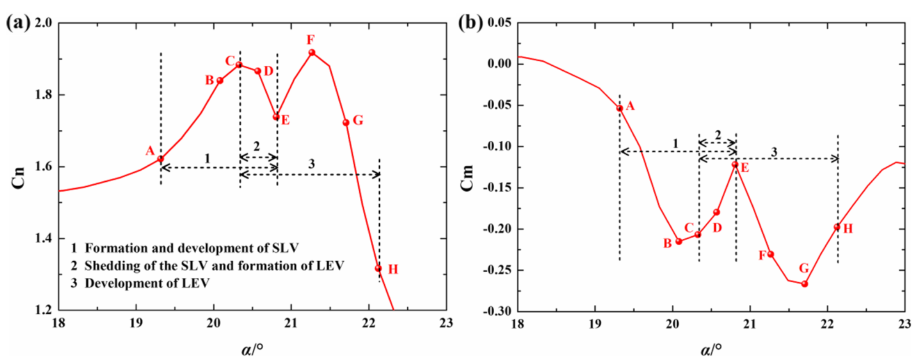

Fig. 7 Aerodynamic performance in dynamic stall for $k=0.035$. **a** C_n, **b** C_m

convection of the vortex. In the spatial-temporal evolution contours of C_p, this change of the suction peak can characterize the transportation of the vortex.

Figure 6 shows the spatial-temporal evolution contour of the experimental C_p during the dynamic stall for $k=0.035$. The convection process of the SLV and DSV could be clearly identified by the spatial-temporal evolution contour of C_p. During the AoA of 19.5° to 20.5°, there was a significant SLV at the position of $x/c=0.4-0.7$, and this SLV induced a suction that increased the C_n at this stage. The convection of the DSV was clearly identified between the AoA of 20° to 22°, and this dynamic stall process brought a second peak to the C_n.

Figure 7 represents the experimental aerodynamic performance during the dynamic stall for $k=0.035$, where (a) is C_n and (b) is C_m. The C_n exhibits an obvious bimodal feature characterized by the maximum at AoAs C and F, and the C_m also exhibits an obvious bimodal feature. Only the phases of the bimodal peaks of C_n and C_m are different. The aerodynamic characteristics are closely related to the pressure field evolutionary history. Thus, the unsteady pressure on the airfoil at several typical AoAs was analyzed in detail. Next, the reasons for choosing these AoAs are briefly explained. In Fig. 7, the most easily selected AoAs are *A*, *B*, *C*, *E*, *F* and *G*. The AoAs *C* and *F* are the two peak positions of C_n, and the AoAs *B* and *G* are the two negative peak positions of C_m. AoA *E* is the minimum position of C_n, and AoA *A* is the position where the slope of C_n and C_m starts to increase significantly. And then, AoAs *D* and *H* can also be easily determined. The AoA *D* is between *C* and *E*, and AoA *H* is an AoA during the process of sharp decrease of C_n and sharp increase of C_m. In conjunction with the spatial-temporal evolution contour of C_p as shown in Fig. 6, the evolution of the unsteady pressure field during dynamic stall for $k=0.035$ could be basically divided into three phases as shown in Fig. 7. The first phase is the formation and development phase of the SLV; the second phase is the formation phase of the LEV; and the third phase is the development phase of the LEV. The first phase overlaps with the second phase, and this phase forms the first peak of C_n and C_m. The second peak of C_n and C_m is formed in the third phase. A detailed analysis of the evolution of unsteady pressure in these three phases is conducted as follows.

Figure 8 illustrates the distributions of the experimental C_p during the dynamic stall $k=0.035$, where (a) is the AoA *A* to *E* and (b) is the AoA *E* to *H*. At AoA *A*, the flow still maintained the attached flow. At AoA *B*, a significant SLV-induced suction was formed at the position of $x/c=0.4-0.7$. This part of suction increased C_n and brought a significant downward moment. With the development of the AoA to *C*, the SLV-induced suction gradually developed toward the trailing edge, while the SLV-induced C_p peak was almost constant. At this AoA, a stronger LEV started to form at the position of $x/c=0.15$. This LEV-induced suction further increased C_n, and balanced out the downward moment induced by the SLV, which increased the C_m as shown in Fig. 7(b). When the AoA increased to *D*, both LEV and SLV gradually developed backward. The LEV-induced suction at the leading edge gradually increased and the SLV-induced suction at the trailing edge gradually decreased. The combined effect caused C_n to decrease and C_m to further increase. It can be seen that the first peak of C_n is brought by the SLV and LEV, and the first negative peak of C_m is brought by the SLV. The difference in phase between the two is caused by the phase difference between the SLV and LEV.

As the AoA developed gradually to *E*, the SLV separated from the trailing edge and the LEV developed further toward the trailing edge with gradually increasing strength. The

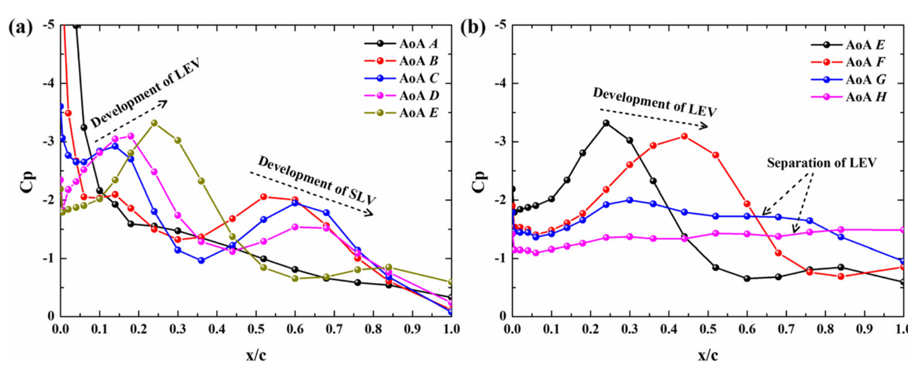

Fig. 8 C_p during dynamic stall for $k=0.035$. **a** AoAs *A* to *E*, **b** AoAs *E* to *H*

separation of the SLV made the upward moment increase further, as shown in Fig. 7(b). And the suction decay from the separation of the SLV was more than that from the enhancement of the LEV, so that the C_n decreased further, as shown in Fig. 7(a). When the AoA developed to *F*, the LEV gradually developed backward with almost the same strength, while the effect range gradually increased, making the C_n gradually increase, as shown in Fig. 7(a). In this process, since the peak of the LEV-induced suction has developed to the position of $x/c>0.25$, the suction brought the downward moment, as shown in Fig. 7(b). With the development of the AoA to *G*, the LEV developed further backward and separated from the airfoil surface. At this time, the suction in the range of $x/c=0.25-0.62$ decreased and the suction at $x/c>0.62$ increased. The increase of suction at the trailing edge was not as large as the decay of suction at the middle section, so the C_n gradually decreased as shown in Fig. 7(a). However, the force arm of suction at the trailing edge was longer, which made the downward moment larger as shown in Fig. 7(b). With the further development of the AoA to *H*, the LEV was almost completely separated from the airfoil surface. The C_n further decreased and the C_m gradually increased as shown in Fig. 7. It can be seen that the second peak of both C_n and C_m is caused by the development of LEV, except that the peak of negative moment of C_m is more dependent on the motion of LEV.

Figure 9 shows the *Q*-criterion contours at different AoAs of the numerical results, which can more intuitively identify the various vortex structures in the dynamic stall and can more favorably support the previous discussion. In the pre-dynamic stall, the wall shear layer developed first. When the LEV cannot maintain its morphology of adhering to the wall, it gradually moved away from the wall. However, its strength and scale were increasing, and the effect range on the C_p of the airfoil was gradually increasing, which could also be reflected in Fig. 8(b). The SLV maintained its scale and intensity almost constant for a period of time and then gradually dissipated at the trailing edge, which could be seen in Fig. 8(a). The development of LEV proceeds in

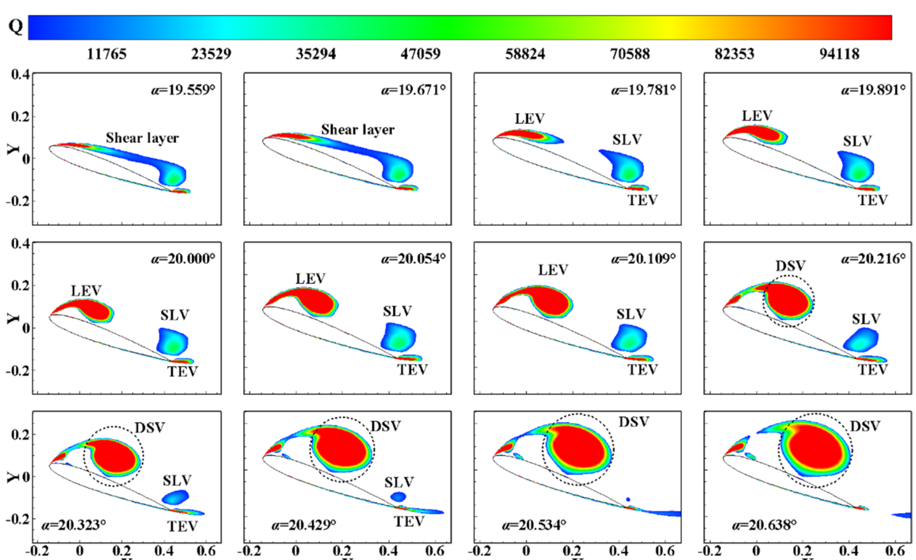

Fig. 9 *Q*-criterion contours at different AoAs for $k=0.035$

parallel with the dissipation of SLV, which is also consistent with the findings in Fig. 8. A smaller scale trailing edge vortex (TEV) was identified in the Q-criterion contour, which cannot be identified in Figs. 6 and 8. This is due to the fact that the TEV does not directly bring C_p changes to the airfoil surface. It is noteworthy that the C_n of the calculated result in Fig. 9 is larger than that of the experimental result as shown in Fig. 4. And this can be attributed to the fact that the vortex-induced lifts of the calculated and experimental results are different for the intensities of the vortex are different. We believe that this phenomenon is caused by the unsteady wall interference effect [1].

The TEV, SLV, LEV and DSV mentioned in this paper are concepts with consensus. The TEV is a vortex structure near the trailing edge. It adsorbs the flow from the lower surface to the upper surface, and then the shear layer here rolls up a vortex, which is fixed near the trailing edge, so it is called the TEV. The SLV is a shear layer vortex which is also called the turbulent separation vortex because of the turbulent separation that occurs at high Reynolds numbers. The LEV can be considered as the initial stage of DSV, and when the LEV cannot maintain the existing scale, it will detach from the leading edge of the airfoil and convect downstream, forming the DSV.

3.2.2 Case of $k = 0.1$

Figure 10 shows the spatial-temporal evolution contour of the experimental C_p during the dynamic stall for $k = 0.1$. The convection process of the DSV could be clearly identified, while no SLV was identified, which was different from the case of $k = 0.035$. The spatial-temporal evolution of C_p shows that a significant dynamic stall occurs in the mid-front part of the airfoil starting from 22° and brings about a significant C_n

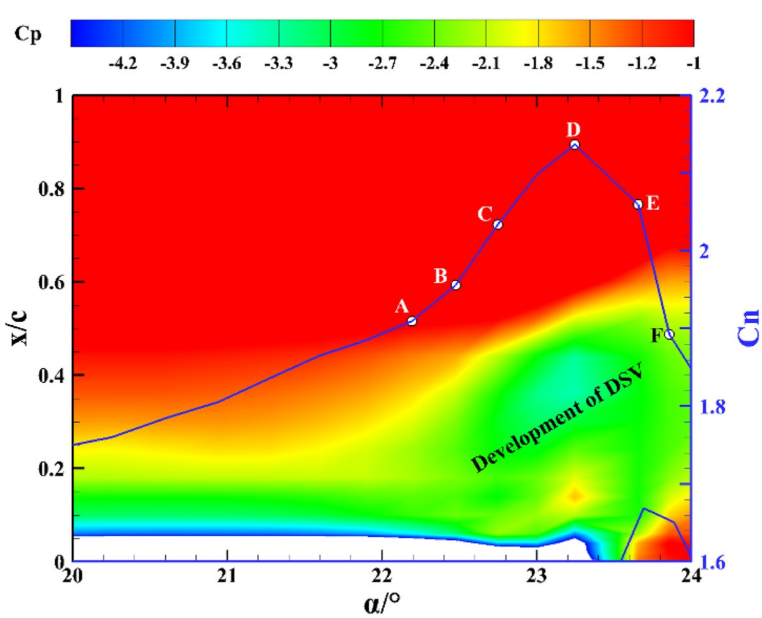

Fig. 10 Spatial-temporal evolution contours of C_p for $k = 0.1$

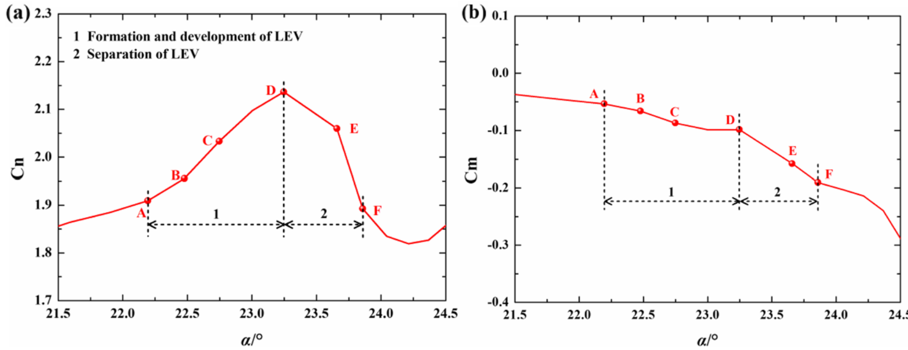

Fig. 11 Aerodynamic performance in dynamic stall for $k=0.1$. **a** C_n, **b** C_m

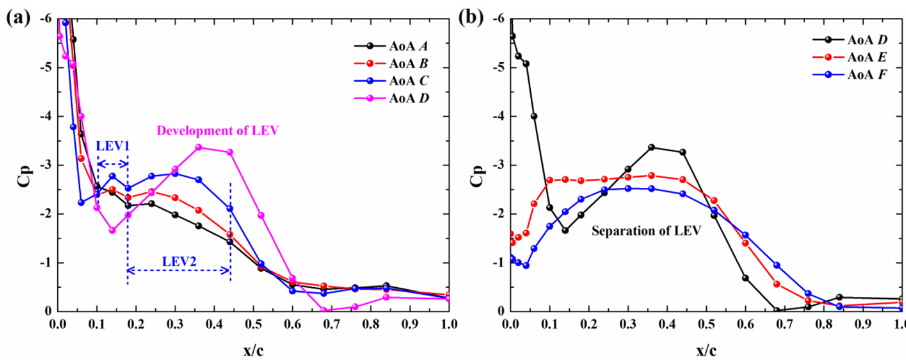

Fig. 12 C_p during dynamic stall for $k=0.1$. **a** AoAs *A* to *D*, **b** AoAs *D* to *F*

enhancement. Unlike the case of $k=0.035$, the C_n at the reduced frequency of $k=0.1$ does not exhibit a bimodal feature.

Figure 11 displays the experimental aerodynamic performance during the dynamic stall for $k=0.1$, where (a) is C_n and (b) is C_m. It is obvious that neither C_n nor C_m has a bimodal feature, which is significantly different from the case of $k=0.035$. In order to better analyze the unsteady pressure field, we still take several typical AoAs of C_p for a detailed discussion. In conjunction with the spatial-temporal evolution contour of C_p as shown in Fig. 10, the evolution of the unsteady pressure field during dynamic stall for $k=0.1$ could be divided into two phases as shown in Fig. 11. The first phase is the formation and development phase of LEV, and the second phase is the LEV separation phase.

Figure 12 illustrates the distributions of the experimental C_p during the dynamic stall for $k=0.1$, where (a) is the AoA *A* to *D* and (b) is the AoA *D* to *F*. At AoA *A*, the flow still maintained the attached flow. At AoA *B*, two weak LEVs called LEV1 and LEV2 were formed at the position of $x/c=0.1-0.45$. The suction brought by the LEV system made C_n increase, and since this part of suction was distributed around $x/c=0.25$, it did not bring a significant change of C_m. With the development of the AoA to *C*, the suction brought by the LEV system gradually increased, making C_n further increased, and since its position hardly changed, C_m still did not change significantly, as shown in Fig. 11(b). The C_p peak at this stage is induced by the LEV system, which can be more visually observed by panels 5–8 in Fig. 13. When the AoA increased to *D*, the LEV1

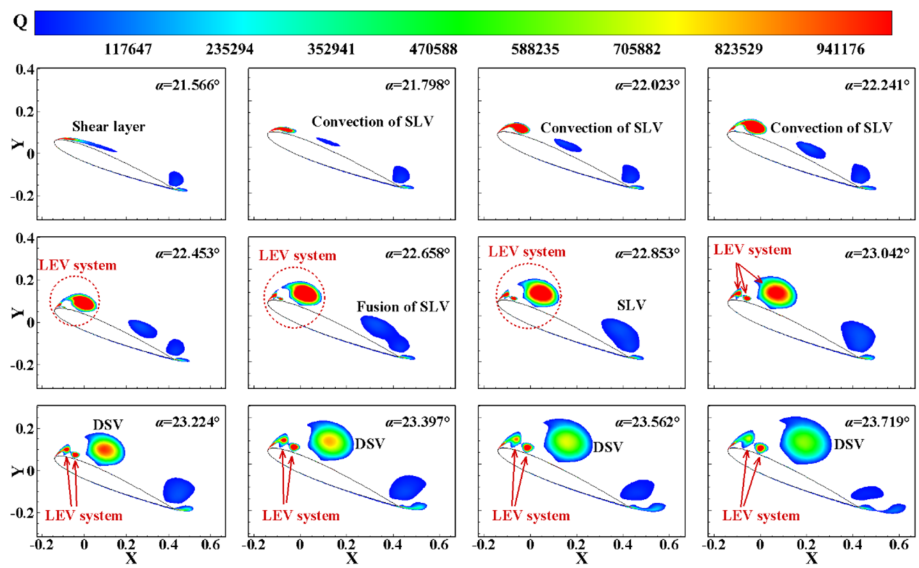

Fig. 13 *Q*-criterion contours at different AoAs for $k = 0.1$

gradually disappeared and the LEV2 further developed, and the induced suction further increased. The increment of suction brought by LEV2 was greater than the decay of suction brought by LEV1; therefore, the C_n further increased and formed a peak, as shown in Fig. 11(a). As the AoA increased to *E*, the peak of the LEV-induced suction gradually decreased, indicating that it gradually detached from the airfoil surface. However, its effect range gradually increased, indicating that the LEV was still gradually strengthened. When the AoA was *F*, the LEV was further separated from the airfoil surface and the induced suction was further reduced. This dynamic stall process was dominated by the convection of the LEV, with a peak in C_n and a continuously varying pattern in C_m.

Figure 13 shows the numerical result of *Q*-criterion contours at different AoAs for $k = 0.1$. In the pre-dynamic stall, the wall shear layer still developed first. The convection of the SLV within the shear layer could be clearly identified. Vortex fusion and dissipation occurred as the SLV developed to the trailing edge. And the suction induced by the SLV causes the first peak of C_n as shown in Fig. 4. However, this SLV was not identified in the image of the spatial-temporal evolution of C_p in the experiment, as shown in Figs. 10 and 12. We believe this is because the SLV in the experiment was not strong enough to induce a sufficient negative C_p peak. The SLV convection process is accompanied by the gradual formation and development of the LEVs, as shown in Fig. 13. Under the effect of continuous accumulation of the bottom layer vorticity, the secondary separation generated multiple LEVs and formed a LEV system which was characterized by the multi-scale. At the phase of full development of the LEV system, three clear LEVs could be identified by the *Q*-criterion contour. In contrast, only two LEVs could be identified in the spatial-temporal evolution image of C_p, and the main vortex structures, however, could be clearly identified. And this LEV system causes the second peak of C_n in the numerical result as shown in Fig. 4. The study in article [1] shows that the presence of wind tunnel walls significantly affects the vortex structure in the dynamic stall of dynamic airfoil. Therefore, this difference between the experimental and calculated results in this paper may be caused by the unsteady wall interference effect.

3.3 Vortex characteristics in dynamic stall

As can be seen from the previous analysis, the vortex structure on the suction surface directly determines the dynamic stall development process. Therefore, the effect of the reduced frequency on the LEV and SLV was further discussed using the experimental results in this section.

Under small reduced frequencies, the evolution of the unsteady pressure field during dynamic stall exhibited similarities and differences. A comparison between the LEV and SLV in the cases of $k=0.035$ and 0.05 is presented in Fig. 14. The LEV and SLV had a significant phase difference under the two reduced frequencies.

Specifically, in the case of $k=0.035$, the LEV began to form and gradually developed from AoA B_1, while the SLV-induced C_p gradually increased. From AoA B_1 to D_1, the LEV enhancement was greater than the SLV attenuation, causing the first peak of C_n. From AoA D_1 to E_1, the degree of SLV attenuation was greater than the degree of enhancement of the LEV, which caused the C_n to gradually decrease. After AoA E_1, the SLV detached from the airfoil surface, while the LEV-induced C_p remained almost unchanged, which caused C_n to increase again, and resulted in a second C_n peak. Moreover, the multi-peak phenomenon of C_m shown in Fig. 7 was also caused by the complex development characteristics of the SLV and LEV.

In the case of $k=0.05$, the SLV induced significant suction before AoA C_2. After AoA C_2, the SLV gradually decayed, and the LEV began to form and develop, which resulted in a maximum value of C_n near this AoA. After AoA D_2, both the LEV and

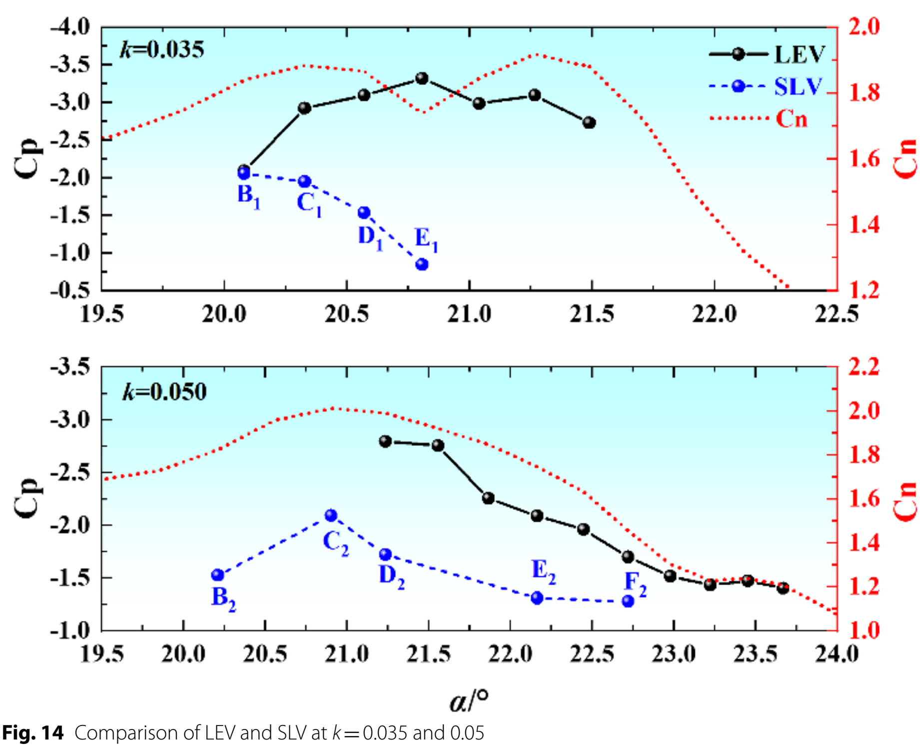

Fig. 14 Comparison of LEV and SLV at $k=0.035$ and 0.05

SLV gradually decayed, and this process was accompanied by a gradual decrease in C_n. After AoA F_2, i.e., after the SLV completely separated from the airfoil surface, the LEV-induced C_p was small, and its intensity was not strong enough to cause C_n to increase significantly again. Thus, there was not a second peak as the case of $k=0.035$.

From the analysis in Fig. 14 and Section 3.2, it is clear that the vortex structure is interrelated with C_n. The intensity changes of the SLV and LEV profoundly affected the aerodynamic performance at small reduced frequencies ($k=0.035$ and 0.05). In the case of the large reduced frequency ($k=0.1$), no SLV was identified in this study, so the LEV directly affected the aerodynamics of the airfoil. In the presence of the SLV ($k=0.035$ and 0.05), the sum of the negative C_p peaks induced by LEV and SLV was used as the total C_p peak, otherwise the negative C_p peak induced by LEV was used as the C_p peak.

The relationship between the C_p peak and the normal force coefficient C_n is shown in Fig. 15. Under different reduced frequencies, there was a significant linear correlation between the C_p peak and C_n. Therefore, the C_p peak directly determines the performance of C_n. The C_m is not only related to the C_p peak value but also directly related to the position of C_p peak. Therefore, there is no simple linear relationship between C_m and the C_p peak.

It is noteworthy that the linear correlation between the negative C_p peak and C_n is weak for $k=0.035$. From a mathematical point of view, the C_n value in dynamic stall phase for $k=0.035$ is around 1.8, which does not show a wide range of variation like the large reduced frequency cases ($k=0.05$ and 0.1). It will lead to a weak linear correlation, both in terms of correlation coefficient and visual perception. From a physical point of view, the C_n is calculated by the integration of C_p and is not only related to the negative C_p peak but also to its distribution. As shown in Fig. 8, a wide range of suction is induced by the LEV for $k=0.035$. So the linear correlation of the C_n and the negative peak of C_p should not be strong.

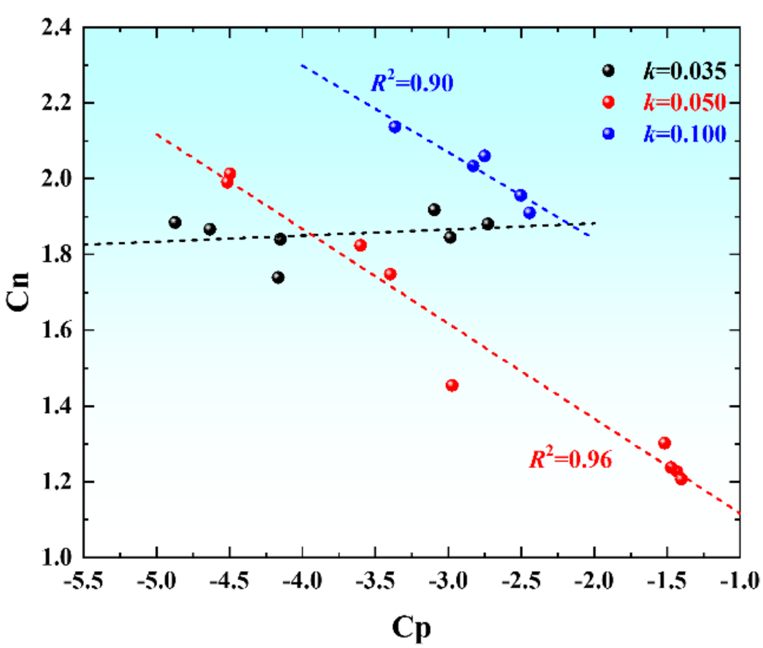

Fig. 15 Linear correlation between C_p peak and C_n

Many semi-empirical models are based on these vortex effects, such as the L-B model [44]. The research in this paper showed that the development characteristics of the C_p peak determined the performance of C_n. And this study also highlighted some limitations of these semi-empirical models, i.e., the traditional L-B model only considers the impact of the LEV. In fact, the development of the LEV and SLV jointly determined the aerodynamic characteristics as discussed in the previous section. This work can provide a certain theoretical basis for the semi-empirical models.

In Theodorsen's linear theory [45], under a small Reynolds number, the maximum lift coefficient is affected by the AoA amplitude and k in the case of small and large k, respectively. Li et al. [2] believed that the Theodorsen theory also had a certain applicability under a transitional Reynolds number of $Re=9\times10^4$. The results presented in this article showed that in the case of a large Reynolds number of $Re=1.5\times10^6$, the reduced frequency had an important effect on the LEV intensity. Theodorsen's linear theory also has a certain applicability in cases with large Reynolds numbers.

3.4 Time-frequency characteristics of dynamic stall

The vortex characteristics of the dynamic stall were analyzed in detail in the previous content. And although the vortex of a whole period is not presented, it is sufficient to analyze the vortex characteristics and the time-frequency characteristics of the dynamic stall. Two reduced frequencies of $k=0.035$ and $k=0.1$ were taken as examples to analyze the time-frequency characteristics of DSV using the experimental results.

3.4.1 Case of k = 0.035

The time-frequency spectrum of C_p at three typical positions of $x/c=0.14$, 0.44 and 0.68 is shown in Fig. 16, where the red solid line is the collected pressure signal. The horizontal axis is the dimensionless time normalized using the oscillation period T by $\tau=t/T$. The AoA D and F identified in the figure correspond to the AoA D and F in Figs. 6, 7 and 8, respectively. Combined with Fig. 8 and the analysis in Section 3.2, it can be seen that in Fig. 16, the negative peak of C_p at position $x/c=0.14$ characterizes a LEV, the first negative peak of C_p at position $x/c=0.44$ characterizes a SLV, and the second negative peak of C_p characterizes a LEV developed from position $x/c=0.14$. The first negative C_p peak at $x/c=0.68$ characterizes the SLV developed from the $x/c=0.44$ position, and the second negative C_p peak characterizes the LEV developed from the leading edge.

The position of $x/c=0.14$ experienced the development and decay of the LEV. The energy of the signal with a frequency component $f\approx200\,\text{Hz}\sim800\,\text{Hz}$ was obviously enhanced when the LEV swept as reflected in the time-frequency spectrum. As the AoA increased to F, the LEV moved to the position of $x/c=0.44$. And the energy with a frequency component of $f\approx200\,\text{Hz}\sim1500\,\text{Hz}$ at this position was significantly strengthened. With the further development of time to $\tau\approx0.38$, the LEV moved to the position at $x/c=0.68$, and the time-frequency spectrum at this position also exhibited a significant broadband feature. Although the position at $x/c=0.44$ underwent the SLV sweeping, there was no energy distribution in the time-frequency spectrum because of its weak intensity. When this SLV swept to $x/c=0.68$, its energy was enhanced by the accumulation of vorticity, and then there was a broadband energy distribution with $f\approx200\,\text{Hz}\sim1500\,\text{Hz}$ in the time-frequency spectrum.

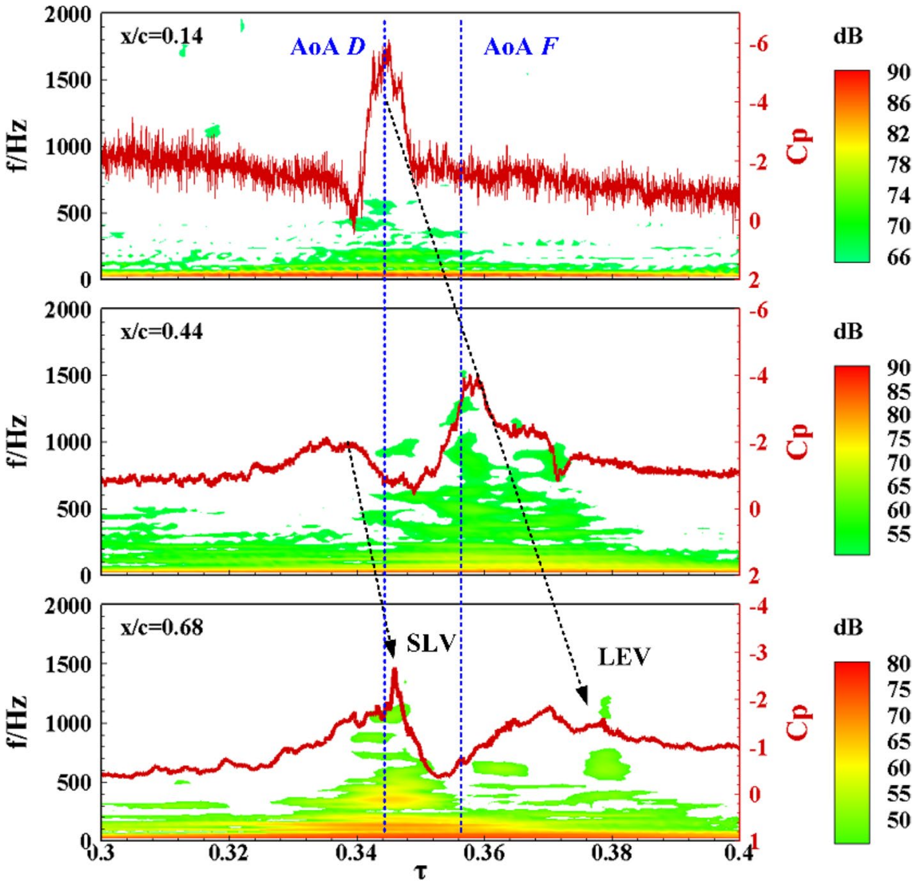

Fig. 16 Time-frequency spectrum in the case of $k = 0.035$

Comparing the SLV at $x/c = 0.68$ with the LEV at $x/c = 0.44$, it can be seen that both SLV and LEV have extremely rich frequency structures, reflecting that both SLV and LEV possess multi-scale structures. From the development process of LEV, the near-wall LEV will first experience frequency enhancement ($x/c = 0.14$–0.44), and then the high-frequency features will gradually decay ($x/c = 0.68$), characterized by that the small-scale structure of LEV will gradually dissipate.

3.4.2 Case of k = 0.1

The time-frequency spectrum of C_p at two typical positions of $x/c = 0.14$ and 0.36 is shown in Fig. 17, where the red solid line is the pressure signal. The AoA *D* and *E* identified in this figure correspond to the AoA *D* and *E* in Figs. 10, 11 and 12, respectively. The negative C_p peaks from the leading edge vortex system at these two positions are significant.

The vortex system at position of $x/c = 0.14$ had a rich frequency structure and exhibited a broad frequency characteristic of $f \approx 200\,\text{Hz} \sim 1800\,\text{Hz}$. The vortex system at position of $x/c = 0.36$ also exhibited a similar broad frequency characteristic. And the LEV system at these two positions occurred at a close time, indicating that the LEV

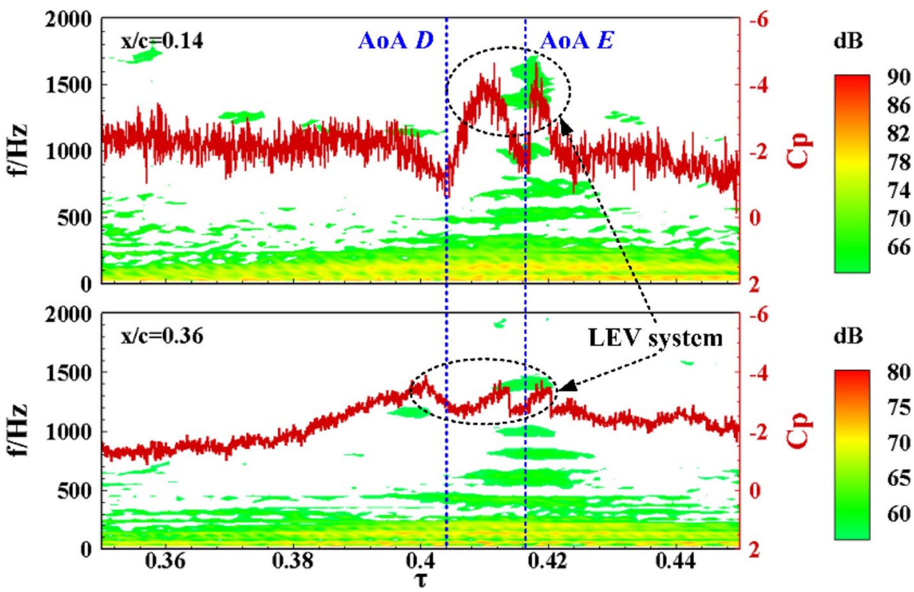

Fig. 17 Time-frequency spectrum in the case of $k=0.1$

system had a large scale and was able to bring a negative peak of C_p for both positions of $x/c=0.14$ and 0.36, which was consistent with the results in Fig. 13.

Comparing the time-frequency spectrum of LEV at the two reduced frequencies, several strip-structures were observed from $f=500$ - 1500 Hz for the large reduced frequency. From the previous analysis about the experimental results, it is clear that only one LEV is formed during the dynamic stall at the small reduced frequency ($k=0.035$), while the LEV system is formed at the large reduced frequency ($k=0.1$). It can be seen that these strip-structures in Fig. 17 for the large reduced frequency are caused by the sweep of the LEV system. In addition, the LEV possesses multi-scale structures, and the multi-scale structures of the LEV become more significant as the reduced frequency gradually increases, characterized by that the LEV in the case of the large reduced frequency possesses a wider spectrum. And the results were consistent with the studies of Pruski and Bowersox [22] and Mulleners et al. [18] They also concluded that the frequency band of LEV was wider as the reduced frequency increased.

4 Conclusion

The dynamic stall physics of the NACA0012 airfoil under a high Reynolds number ($Re \sim O(10^6)$) and a high reduced frequency ($k \sim O(10^{-1})$) was studied using experimental and numerical methods. The experimental Reynolds number was $Re=1.5\times10^6$, and the reduced frequency range was $k=0.035-0.1$. The average AoA and the amplitude of the pitching oscillation was 15° and 10°, respectively.

A detailed study of the unsteady flow field in dynamic stall was carried out using the transient pressure measurement and the numerical simulation based on the URANS. At a reduced frequency of $k=0.035$, the aerodynamic performance during the dynamic stall is dominated by the SLV and LEV, where the SLV and LEV-induced suction determines the C_n, while the C_m is related to the kinematic characteristics of the SLV and LEV. And the dynamic stall field is dominated by the LEV system at a reduced frequency of $k = 0.1$.

An in-depth study of the vortex characteristics of the dynamic stall in the experiment was carried out. There is a significant phase difference between the SLV and the LEV at the reduced frequencies of $k = 0.035$ and 0.05, and this phase difference is a key factor in determining the existence of the bimodal characteristics of the aerodynamic force/moment. There is a significant linear correlation between the negative peak of the vortex-induced C_p and the C_n in the reduced frequency range studied in this paper.

The time-frequency characteristics of the dynamic stall in the experiment were studied in detail using the wavelet analysis. Both the SLV and the LEV possess multi-scale structures. During the convection of the near-wall LEV to the trailing edge, the high-frequency features firstly decay, characterized by that the small-scale structures of LEV gradually dissipate. And the multi-scale structures of the LEV become more significant as the reduced frequency gradually increases, characterized by that the LEV in the case of the large reduced frequency possesses a wider frequency spectrum.

Acknowledgements
We would like to thank all the experimental staff of the NF-3 Wind Tunnel for their hard work.

Authors' contributions
Binbin Wei: Analysis, Writing, Reviewing, Editing and Funding acquisition. Yongwei Gao and Shuling Hu: Methodology, Supervision. All authors read and approved the final manuscript.

Funding
This work was supported by the Key Laboratory of Flow Visualization and Measurement Techniques, AVIC Aerodynamics Research Institute (XFX20220502) and the foundation of National Key Laboratory of Science and Technology on Aerodynamic Design and Research (No. 61422010401).

Availability of data and materials
The data presented in this study are available from the corresponding author upon reasonable request.

Declarations

Competing interests
The authors declare that they have no competing interests regarding this work.

Received: 6 December 2022 Accepted: 28 February 2023
Published online: 08 May 2023

References

1. Wei BB, Gao YW, Hu SL (2022) Scale effect during the dynamic stall of dynamic airfoil. Phys Fluids 34:087122
2. Li Z, Feng L, Karbasian HR et al (2019) Experimental and numerical investigation of three-dimensional vortex structures of a pitching airfoil at a transitional Reynolds number. Chin J Aeronaut 32(10):2254–2266
3. Buchner AJ, Honnery D, Soria J (2017) Stability and three-dimensional evolution of a transitional dynamic stall vortex. J Fluid Mech 823:166–197
4. Fuchiwaki M, Tanaka K (2010) Vortex structure in unsteady separation around a pitching airfoil. Ann N Y Acad Sci 972(1):61–66
5. Buchner AJ, Buchmann N, Kilany K et al (2012) Stereoscopic and tomographic PIV of a pitching plate. Exp Fluids 52(2):299–314
6. Widmann A, Tropea C (2017) Reynolds number influence on the formation of vortical structures on a pitching flat plate. Interface Focus 7(1):20160079
7. Mackowski AW, Williamson CHK (2015) Direct measurement of thrust and efficiency of an airfoil undergoing pure pitching. J Fluid Mech 765:524–543
8. Kim DH, Chang JW (2014) Low-Reynolds-number effect on the aerodynamic characteristics of a pitching NACA0012 airfoil. Aerosp Sci Technol 32(1):162–168
9. Yu HT, Bernal LP (2017) Effects of pivot location and reduced pitch rate on pitching rectangular flat plates. AIAA J 55(3):702–718
10. Lee T, Gerontakos P (2004) Investigation of flow over an oscillating airfoil. J Fluid Mech 512:313–341
11. Soylak M (2016) Experimental investigation of aerodynamic performance of oscillating wings at low Re numbers. Proc Inst Mech Eng G J Aerosp Eng 230(10):1882–1902

12. Taylor K, Amitay M (2015) Dynamic stall process on a finite span model and its control via synthetic jet actuators. Phys Fluids 27(7):077104
13. Mulleners K, Raffel M (2013) Dynamic stall development. Exp Fluids 54:1469
14. Lorber P, Carta FO (1987) Airfoil dynamic stall at constant pitch rate and high Reynolds number. Paper presented at the 19th AIAA, fluid dynamics, plasma dynamics, and lasers conference, Honolulu, 8-10 June 1987
15. Acharya M, Metwally MH (1992) Unsteady pressure field and vorticity production over a pitching airfoil. AIAA J 30(2):403–411
16. Karim MA, Acharya M (1993) Control of the dynamic-stall vortex over a pitching airfoil by leading-edge suction. Paper presented at the 3rd shear flow conference, Orlando, 6-9 July 1993
17. Geissler W, Dietz G, Mai H et al (2005) Dynamic stall and its passive control investigations on the OA209 airfoil section. In: 31th European rotorcraft forum, Florence, September 2005. vol 1. Associazione Italiana de Aerotecnica e Astronautica, pp 1134–1151
18. Mulleners K, Henning A, Mai H et al (2009) Investigation of the unsteady flow development over a pitching airfoil by means of TR-PIV. Paper presented at the 27th AIAA applied aerodynamics conference, San Antonio, 22-25 June 2009
19. Gardner AD, Richter K, Mai H et al (2013) Experimental investigation of dynamic stall performance for the EDI-M109 and EDI-M112 airfoils. J Am Helicopter Soc 58(1):1–13
20. Worasinchai S, Ingram G, Dominy R (2013) Unsteady surface pressures and airload of a pitching airfoil. Energy Procedia 34:407–416
21. Rasi Marzabadi F, Soltani MR (2012) Experimental study of the boundary layer over an airfoil in plunging motion. Acta Mech Sin 28:372–384
22. Pruski BJ, Bowersox RDW (2013) Leading-edge flow structure of a dynamically pitching NACA 0012 airfoil. AIAA J 51(5):1042–1053
23. Ajalli F, Mani M (2014) Effects of adding strip flap on a plunging airfoil. Aircr Eng Aerosp Technol 86(1):6–18
24. Melius M, Cal RB, Mulleners K (2016) Dynamic stall of an experimental wind turbine blade. Phys Fluids 28(3):034103
25. Lind AH, Jones AR (2016) Unsteady aerodynamics of reverse flow dynamic stall on an oscillating blade section. Phys Fluids 28(7):077102
26. Gupta R, Ansell PJ (2019) Unsteady flow physics of airfoil dynamic stall. AIAA J 57(1):165–175
27. Deparday J, Mulleners K (2019) Modeling the interplay between the shear layer and leading edge suction during dynamic stall. Phys Fluids 31(10):107104
28. Gardner AD, Richter K (2020) Effect of the model-sidewall connection for a dynamic stall airfoil experiment. J Aircr 57(1):173–178
29. Sarkar S, Venkatraman K (2008) Influence of pitching angle of incidence on the dynamic stall behavior of a symmetric airfoil. Eur J Mech B Fluids 27(3):219–238
30. Rosti ME, Omidyeganeh M, Pinelli A (2016) Direct numerical simulation of the flow around an aerofoil in ramp-up motion. Phys Fluids 28(2):025106
31. Guillaud N, Balarac G, Goncalvès E (2018) Large eddy simulations on a pitching airfoil: analysis of the reduced frequency influence. Comput Fluids 161:1–13
32. Karbasian HR, Kim KC (2016) Numerical investigations on flow structure and behavior of vortices in the dynamic stall of an oscillating pitching hydrofoil. Ocean Eng 127(10):200–211
33. Motta V, Guardone A, Quaranta G (2015) Influence of airfoil thickness on unsteady aerodynamic loads on pitching airfoils. J Fluid Mech 774:460–487
34. Tseng CC, Cheng YE (2015) Numerical investigations of the vortex interactions for a flow over a pitching foil at different stages. J Fluids Struct 58:291–318
35. Gharali K, Johnson DA (2014) PIV-based load investigation in dynamic stall for different reduced frequencies. Exp Fluids 55:1803
36. Zanotti A, Melone S, Nilifard R et al (2013) Experimental-numerical investigation of a pitching airfoil in deep dynamic stall. Proc Inst Mech Eng G J Aerosp Eng 228(4):557–566
37. Soltani MR, Seddighi M, Rasi Marzabadi F (2009) Comparison of pitching and plunging effects on the surface pressure variation of a wind turbine blade section. Wind Energy 12(3):213–239
38. Jain R, Le Pape A, Grubb A et al (2018) High-resolution computational fluid dynamics predictions for the static and dynamic stall of a finite-span OA209 wing. J Fluids Struct 78:126–145
39. Chiereghin N, Cleaver DJ, Gursul I (2019) Unsteady lift and moment of a periodically plunging airfoil. AIAA J 57(1):208–222
40. Wei BB, Gao YW, Wang L et al (2019) Analysis of flow transition and separation on oscillating airfoil by pressure signature. J Mech Sci Techniques 33(1):279–288
41. Wei BB, Gao YW, Li D (2021) Physics of dynamic stall vortex during pitching oscillation of dynamic airfoil. Int J Aeronaut Space Sci 22:1263–1277
42. McAlister KW, Pucci SL, McCroskey WJ et al (1982) An experimental study of dynamic stall on advanced airfoil sections. Volume 2. Pressure and force data. NASA Tech Memo NASA-TM-84245-VOL-2
43. Benton SI, Visbal MR (2019) The onset of dynamic stall at a high, transitional Reynolds number. J Fluid Mech 861:860–885
44. Leishman JG, Beddoes TS (1989) A semi-empirical model for dynamic stall. J Am Helicopter Soc 34(3):3–17
45. Theodorsen T (1949) General theory of aerodynamic instability and the mechanism of flutter. NACA Tech Rep NACA-TR-496

Publisher's Note